







RESEARCH ARTICLE | APRIL 08 2025

## Harvesting sustainable energy through vortex-induced vibrations of finite length cylinder

Andrei Fershalov ; Niell Elvin ; Pieter Orlandini ; Ilya Avros ; Yang Liu  



*Physics of Fluids* 37, 044108 (2025)

<https://doi.org/10.1063/5.0260317>

 CHORUS



View  
Online



Export  
Citation



Physics of Fluids

Special Topics Open  
for Submissions

[Learn More](#)

# Harvesting sustainable energy through vortex-induced vibrations of finite length cylinder

Cite as: Phys. Fluids **37**, 044108 (2025); doi: [10.1063/5.0260317](https://doi.org/10.1063/5.0260317)

Submitted: 23 January 2025 · Accepted: 24 March 2025 ·

Published Online: 8 April 2025



Andrei Fershalov, Niell Elvin, Pieter Orlandini, Ilya Avros, and Yang Liu<sup>a)</sup>

## AFFILIATIONS

Department of Mechanical Engineering, The City College of New York, New York, New York 10031, USA

<sup>a)</sup> Author to whom correspondence should be addressed: [yliu7@ccny.cuny.edu](mailto:yliu7@ccny.cuny.edu)

## ABSTRACT

Vortex-induced vibration (VIV) has emerged as a promising method for small-scale energy harvesting. This research explores the key parameters affecting VIV in a cylinder-cantilever beam system within a Reynolds number range of 400–7500. The investigation focused on identifying the airflow velocity thresholds that initiate vibrations, measuring peak vibration amplitudes, and determining the critical airflow velocities where vibrations are maximized. By systematically varying mass, stiffness, and cylinder diameter, we examined their distinct effects on system behavior. Key outcomes indicate that larger cylinder diameters lead to increased vibration amplitudes and broader operational bandwidths, while adding mass reduces the bandwidth. Higher stiffness boosts both the maximum amplitude and bandwidth, shifting these to higher airflow velocities. The lock-in regime was observed to initiate at a Strouhal number ( $St$ ) between 0.175 and 0.197, with vibration cessation occurring at an approximately consistent Strouhal number for each cylinder diameter. The peak vibration amplitude occurred at  $St \approx 0.16$ , with fluctuations of less than 5% across all models. Additionally, the wake structure behind the cylinder and its behavior across the vibration bandwidth were analyzed using flow visualization techniques. A hot-wire anemometer positioned downstream measured velocity fluctuations from vortex shedding. These findings offer practical insights for optimizing VIV-based energy harvesting, linking wake behavior to amplitude response and power output. This study contributes to the broader understanding of VIV energy harvesters and provides a foundation for validating numerical models and enhancing the efficiency of sustainable energy systems.

Published under an exclusive license by AIP Publishing. <https://doi.org/10.1063/5.0260317>

## NOMENCLATURE

$A$	Amplitude of vibration (m)	$L_b$	Length of the beam (m)
$A^*$	Amplitude ratio	$L_b/D$	Beam length to cylinder diameter ratio
$AR$	Cylinder aspect ratio	$l_0$	Distance between the beams' fixed end and the piezoelectric patch (m)
$C_A$	The ideal added mass coefficient	$l_p$	Length of the piezoelectric patch (m)
$C_p$	Piezoelectric capacitance (F)	$m^*$	Mass ratio
$c$	Structural damping (kg/s)	$m_v$	Vibrating mass (kg)
$D$	Diameter of the cylinder (m)	$P$	The instantaneous electrical power (W)
$d_{31}$	Piezoelectric constant (pm/V)	$P_{opt}$	The optimal power (W)
$f$	Vibration frequency (Hz)	$P^*$	Dimensionless power
$f_n$	Natural frequency of the vibrating structure (Hz)	$\bar{P}$	The average electrical power (W)
$f_v$	Vortex shedding frequency (Hz)	$R$	Electrical resistance ( $\Omega$ )
$h_b$	Height of the beam (m)	$R_{opt}$	Optimal electrical resistance ( $\Omega$ )
$h_p$	Height of the piezoelectric patch (m)	$Re$	Reynolds number
$i_p$	Piezoelectric current (A)	$St$	Strouhal number
$k$	Structural stiffness (N/m)	$T$	Vibration period (s)
$k_{33}^{-S}$	Permittivity under constant strain (nF/m)	$t$	Time (s)
$L$	Length of the cylinder (m)	$t_b$	Thickness of the beam (m)
		$t_p$	Thickness of the piezoelectric patch (m)

$U$	Absolute velocity (m/s)
$U_c$	Cylinder velocity in cross-flow direction (m/s)
$U_\infty$	Free stream velocity (m/s)
$U^*$	Reduced velocity
$V_L$	Voltage magnitude across a load resistance (V)
$V_{L_{opt}}$	Optimal voltage magnitude across a load resistance (V)
$\bar{V}_p$	Voltage magnitude generated by the piezoelectric material (V)
$v_L$	Voltage across a load resistance (V)
$Y_p$	Elastic modulus of the piezoelectric patches (GPa)
$y$	Deflection of the beam tip (m)
$\alpha$	Angle between absolute velocity and free stream velocity ( $^\circ$ )
$\varepsilon_p$	Strain at the half-thickness of the piezoelectric patch
$\zeta$	Damping ratio
$\theta$	Electromechanical coupling coefficient (N/V)
$\nu$	Kinematic viscosity of the fluid ( $\text{m}^2/\text{s}$ )
$\rho$	Fluid density ( $\text{kg}/\text{m}^3$ )
$\omega$	Angular frequency (rad/s)
$\omega_n$	Angular natural frequency (rad/s)
$\Delta U$	Bandwidth of vibration (m/s)

## I. INTRODUCTION

Vortex-induced vibration (VIV) is a complex fluid–structure interaction phenomenon that occurs when unsteady vortices shed from a bluff body, such as a circular cylinder, leading to oscillatory forces and vibration of the supporting structure.<sup>1</sup> As the flow continues past the cylinder, alternating vortices are formed—a process known as vortex shedding—that can induce vibrations. VIV becomes particularly significant when the frequency of vortex shedding approaches the natural frequency of the structure, potentially leading to large oscillations. This synchronization, known as the lock-in phenomenon, occurs over a specific range of reduced velocities and can significantly amplify the oscillations in the system.<sup>2–4</sup>

The vortex shedding effect on a vibrating system has been extensively investigated by various researchers.<sup>2,4–9</sup> It has been observed that the motion of the body can influence the instability mechanism that results in vortex shedding. Consequently, the flow generated by vortex shedding around a vibrating bluff body exhibits notable differences from that around a fixed one.<sup>2</sup>

Historically, VIV has been treated as a problem to be avoided, as excessive vibrations can lead to structural fatigue and failure. However, recent research has shifted toward exploring VIV as a method for harvesting energy from fluid flows, driven by advances in low-power electronics and the increasing demand for sustainable energy solutions.<sup>10–13</sup> The use of piezoelectric materials has opened new pathways for converting mechanical vibrations into electrical energy, particularly for small-scale applications, such as remote sensors.<sup>14,15</sup> Fluid–structure interactions in energy harvesting systems are highly dependent on both the dynamics of the flow and the structural response, making the study of VIV critical in understanding and optimizing these systems.

Researchers, such as Allen and Smits<sup>16</sup> pioneered the study of fluidic energy harvesting by examining piezoelectric beams in oscillatory flows. Their work demonstrated how flexible beams in fluid wakes can be used to generate electrical energy. Taylor *et al.*<sup>17</sup> and Yang *et al.*<sup>18</sup> later expanded these concepts to ocean waves, illustrating the versatility of piezoelectric materials in harvesting energy from fluid motion. Anton and Sodano<sup>19</sup> further reviewed advances in piezoelectric energy

harvesting, highlighting significant progress in capturing mechanical vibrations for power generation. Akaydin *et al.*<sup>20,21</sup> explored energy harvesting from highly unsteady fluid flows, emphasizing how fluid–structure interactions could increase power generation by utilizing the motion of bluff bodies in turbulent environments. Azadeh-Ranjbar *et al.*<sup>12</sup> investigated vortex-induced vibrations of finite-length cylinders, revealing how the aspect ratio (AR) influences the lock-in regime and broadens the effective energy harvesting envelope. Goushcha *et al.*<sup>22</sup> examined turbulent boundary layers, showcasing how vortex shedding and wake dynamics enhance energy extraction using piezoelectric materials.

Recent studies have introduced innovative designs and configurations to further optimize piezoelectric-based VIV harvesters. For instance, research into slit-offset circular cylinders has demonstrated significant amplification of VIV amplitudes, enhancing energy harvesting efficiency at low Reynolds numbers.<sup>23,24</sup> Hybrid systems combining piezoelectric and electromagnetic transduction mechanisms have also shown improved energy harvesting performance under VIV conditions.<sup>25,26</sup> Comprehensive reviews have summarized advancements in flow-induced piezoelectric vibration energy harvesting, emphasizing novel mechanisms and emerging applications.<sup>27,28</sup> Experimental studies have verified practical approaches for optimizing piezoelectric energy harvesters employing circular cylinders.<sup>29–31</sup> Additionally, aerodynamic modifications to circular cylinders have been explored to improve aeroelastic instability and efficiency in wind-based energy harvesters utilizing VIV.<sup>32</sup> Recently, research has also explored multi-directional and multi-modal VIV systems, highlighting their potential for significantly enhancing energy harvesting efficiency from wind flows.<sup>33</sup>

Williamson and Govardhan<sup>4</sup> provided an extensive overview of VIV research, detailing amplitude branches and hysteretic transitions. Khalak and Williamson<sup>34–36</sup> characterized various VIV responses, including initial, upper, and lower oscillation branches. Gabbai and Benaroya<sup>6</sup> proposed a first-principles approach using Hamilton’s principle for deriving wake-body models for VIV, offering a physical foundation. Tamura<sup>9</sup> highlighted nonlinear features, such as self-excited vibration, frequency lock-in, and delayed resonance, noting increased amplitude response during lock-in.

The dynamic response of a cylinder with spanwise free-ends, subjected to periodic vortex shedding and tip vortices, depends significantly on the aspect ratio (AR), defined as the cylinder length-to-diameter ratio.<sup>37,38</sup> Additionally, studies of cylinders with one spanwise free-end have characterized “end-cell-induced vibration (ECIV),” a distinct phenomenon occurring alongside VIV at higher wind speeds.<sup>39</sup> Vortex shedding is less pronounced for bluff bodies with lower AR, although it does not completely vanish. Bodies with smaller aspect ratios exhibit weaker vortex shedding, limiting their potential for significant oscillations.<sup>2,38</sup> In our research, we examine cylinders with aspect ratios ranging from 10 to 20.

Energy harvesting applications for cylindrical oscillators typically target airflow velocities between 0 and 2 m/s, aligning with typical wind speeds encountered in outdoor and indoor environments, such as heating, ventilation, and air conditioning (HVAC) systems. Effective energy harvesting within this velocity range is crucial for powering small-scale sensors and devices. The generated power by piezoelectric harvesters depends on the square of displacement amplitude, underscoring the importance of maximizing beam deflection. In energy harvesting applications, not only is the amplitude of vibration

crucial, but also the bandwidth of vibration ( $\Delta U$ ) is equally important. The bandwidth of vibration refers to the range of airflow speeds within which the system undergoes sustained vibrations. This range defines the interval of airflow speeds over which the system remains in resonance or lock-in, allowing for continuous oscillations and energy harvesting. A broader bandwidth of vibration indicates a greater adaptability of the system to varying airflow velocities, enhancing its potential for practical applications in environments with fluctuating airflow conditions. This concept is analogous to the cut-in and cut-out wind speeds in wind turbine applications. The cut-in speed represents the minimum wind speed required to initiate power generation, while the cut-out speed defines the maximum wind speed at which the turbine safely operates. Similarly, the bandwidth of vibration in energy harvesters represents the air velocity range within which the system effectively generates energy. Expanding this bandwidth ensures that the harvester remains operational across a broader range of airflow conditions, thereby increasing its reliability and energy output under variable wind environments.

In this study, we aim to deepen the understanding of the interactions between fluid flow, structural mechanics, and energy harvesting potential. Specifically, we investigate a model system consisting of a circular cylinder attached to a cantilever beam subjected to steady airflow [Fig. 1(a)], allowed to vibrate in a crossflow direction. This system has been examined by several researchers in the past,<sup>10–13</sup> with particular focus on VIV responses, such as initial, upper, and lower branches of oscillation, as observed in the seminal work of Khalak and Williamson.<sup>34–36</sup> Building on this foundation, our work focuses on the experimental characterization of the effects of three key parameters: cylinder diameter, system stiffness, and vibrating mass, on the performance of this energy-harvesting system.

An essential aspect of our investigation involves studying the flow structure behind the cylinder, as the wake is directly affected by vortex shedding and, consequently, the vibration characteristics. To achieve this, we employed advanced flow visualization techniques using fog tracer particles, continuous laser illumination, and high-speed cameras, which allowed us to capture the wake patterns and observe the flow behavior in real time. Additionally, a hot-wire anemometer was installed downstream of the cylinder to measure fluctuations in airflow velocity due to vortex shedding. These techniques are crucial in understanding the fluid dynamics behind the cylinder, as the wake structure not only determines the amplitude and frequency of vibrations but also offers insights into optimizing the energy harvesting efficiency of VIV systems.

This paper presents the experimental results that highlight the importance of key system parameters, including cylinder diameter, system stiffness, and mass, in governing the VIV response. The findings from this research contribute to the broader understanding of VIV as a promising mechanism for small-scale energy harvesting and offer practical insights into optimizing such systems for enhanced performance.

## II. THEORETICAL BACKGROUND

The VIV phenomenon is usually observed when the Reynolds number ( $Re$ ), which is defined as  $Re = \frac{U_\infty D}{\nu}$ , where  $U_\infty$  is the uniform flow velocity,  $D$  is the diameter of the cylinder, and  $\nu$  is the kinematic viscosity of the fluid, exceeds a critical threshold of approximately  $Re = 40$ .<sup>1</sup>

The reduced velocity  $U^* = \frac{U_\infty}{f_n D}$ , where  $f_n$  is the natural frequency of the vibrating structure, plays a key role in defining the lock-in regime. Additionally, the mass ratio  $m^* = \frac{m_v}{\rho \pi D^2 L / 4}$  and damping ratio  $\zeta = \frac{c}{2\sqrt{m_v k}}$ , where  $m_v$  is the vibrating mass,  $\rho$  is the fluid density,  $L$  is the length of the cylinder,  $c$  is the structural damping, and  $k$  is the structural stiffness, are critical parameters influencing the VIV response. The first natural frequency ( $f_n$ ) of the vibrating system can be approximated by  $f_n = \frac{1}{2\pi} \sqrt{\frac{k}{m_v}}$ .

To calculate the average power generated by a piezoelectric energy harvester, the relationship between the beam tip movement and the voltage generated across the piezo element must be considered. The deflection of a piezoelectric beam ( $y$ ) is proportional to the voltage ( $V_p$ ) generated by the piezoelectric material, as given by the simplified relationship  $V_p = -\frac{\theta}{C_p} y$ , where  $C_p$  is the piezoelectric capacitance and  $\theta$  is the electromechanical coupling coefficient.<sup>20</sup> The instantaneous electrical power ( $P$ ) over a resistor is calculated as  $P = \frac{V_L^2}{R}$ , where  $V_L$  is the voltage across a load resistance  $R$ . The average electrical power ( $\bar{P}$ ) over a time ( $t_1 - t_0$ ) period is then defined as  $\bar{P} = \frac{1}{t_1 - t_0} \int_{t_0}^{t_1} P dt$ .

A stationary cylinder placed in the airflow induces vortex shedding [Fig. 1(b)], and the shedding frequency ( $f_v$ ) depends on both the upstream airflow velocity and the cylinder diameter. This relationship can be expressed through the Strouhal number,<sup>40</sup>  $St = \frac{f_v D}{U_\infty}$ . For a stationary cylinder, it is well known that at Reynolds numbers ( $Re$ ) of 1000 and higher,  $St$  remains constant at around 0.18–0.2.<sup>2</sup> This constant  $St$  implies that an increase in airflow velocity leads to a proportional increase in vortex shedding frequency.

However, for a cylinder that is allowed to vibrate in the crossflow direction, the so-called “lock-in” phenomenon occurs in which the frequency of the vortex shedding matches the natural frequency of the system over a relatively wide range of airflow velocities, i.e., the  $St$  decreases with increasing airflow velocity over this lock-in range. Outside the lock-in regime, however, the vortex shedding frequency approximately matches the vortex shedding frequency for the flow passing a stationary cylinder.<sup>2,36</sup> Figure 2 shows a typical amplitude response ( $A$ ) of a vibrating cylinder with increasing airflow velocity (the details of this experiment will be discussed below).

Initially, the cylinder is at rest and as the incoming airflow velocity increases, the vortex shedding frequency increases; the cylinder starts to vibrate as the vortex shedding frequency approaches the structural natural frequency of the system. The vibration amplitude increases rapidly as the vortex shedding frequency nears the structural resonance of the system at which point the system enters the “lock-in” regime. During lock-in, the cylinder experiences large vibration amplitudes. Along with the large amplitude response observed during the lock-in regime, there is a notable effect where the vortex shedding frequency ( $f_v$ ) synchronizes with the natural frequency of the system ( $f_n$ ).<sup>4</sup> This synchronization is a defining characteristic of the lock-in regime and allows for resonance between the fluid forces and the structural vibrations in a wide range of airflow velocities. During this phase, the Strouhal number can be calculated using the formula  $St = \frac{f D}{U_\infty}$ , where  $f = f_n = f_v$ .

As the upstream fluid velocity further increases, there is a jump in vortex shedding frequency, marking the end of the lock-in regime. In the post-lock-in regime, the vortex shedding frequency once again follows the constant Strouhal number law.<sup>12,41,42</sup>



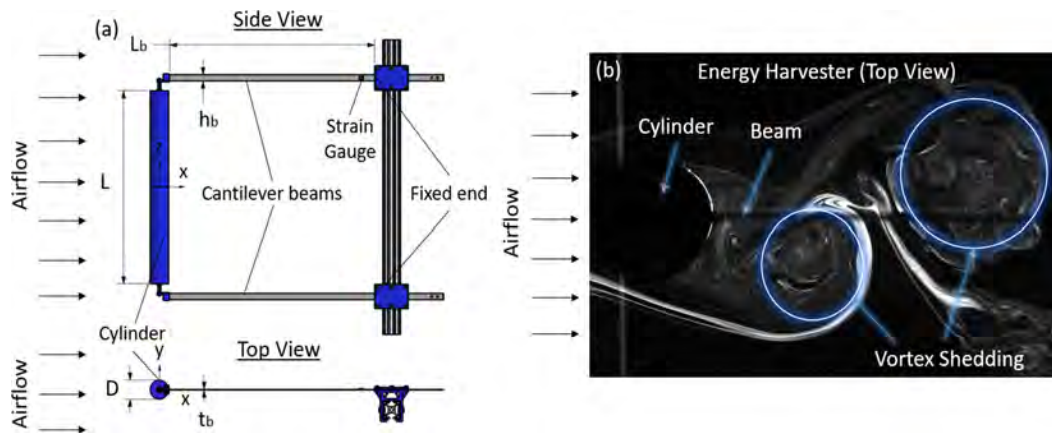


FIG. 1. Energy harvesting system: (a) harvester configuration and (b) vortex shedding behind a cylinder.

Vibrating piezoelectric systems subjected to harmonic excitation are well-understood, and the generated power can be shown to be proportional to the square of the amplitude of the displacement.<sup>43</sup> The coupling between the fluid-flow and the structural system that causes this displacement, however, is not well understood since it involves a complex interaction of vortex-shedding around a moving bluff-body. The goal of the present research is to investigate the effects of critical structural parameters (i.e., mass and stiffness) and geometric parameters (i.e., cylinder diameter) on the amplitude response of a model bluff-body vibrating system.

### III. MATERIALS AND METHODS

Figure 3 depicts the schematic and specific details of the energy harvester utilized in this study. The harvester's configuration allows for the replacement of the bluff body at the end of the cantilevers by different diameters ( $D$ ) of cylinders, the adjustment of stiffness ( $k$ ) by modifying the length of the beams ( $L_b$ ), and the adjustments of vibrating mass ( $m_v$ ).

The cylinder was supported by two beams positioned at the top and bottom ends, outside the wake region, to reduce potential interference with the airflow. To further minimize the impact of these supports on the wake flow and the system's vibrations, the beams were shielded from the airflow by hoods (Fig. 4).

The aluminum beams have the following characteristics: a density of  $2730 \text{ kg/m}^3$ , an elastic modulus of  $69 \text{ GPa}$ , a width of  $12.5 \text{ mm}$ , a thickness of  $1.5 \text{ mm}$ , and an adjustable length ranging from  $450$  to  $550 \text{ mm}$ .

A strain gauge, bonded near the clamped end of one beam, is used to capture the strain in the beam. Calibration was performed to correlate strain gauge readings (in volts) with beam displacement (in millimeters) and to determine the system's static stiffness for each beam length. A custom-built jig enabled the application of known forces to the system in the  $Y$  direction while measuring the displacement of the cylinder axis in the same direction. During each calibration, nine data points were recorded, including the zero position (no force applied) and four points in each positive and negative  $Y$  direction. As expected, the results showed a near-perfect linear relationship between force and displacement ( $r^2 > 0.999$  for all cases), as well as between strain gauge readings and displacement ( $r^2 > 0.999$  for all cases). The slope of the force-displacement dataset allowed for the

determination of the system's static stiffness ( $k$ ) and allowed strain gauge output to be converted to cylinder displacement. The strain gauge was connected to a strain indicator "MM120-001469" (Micro-Measurements Inc.). The output from the strain indicator was recorded using a MATLAB interface via an NI-6008 (National Instruments Inc.) data acquisition card at a  $1000 \text{ Hz}$  sampling rate. The recorded data were then used to calculate the amplitude and frequency of vibration. The strain gauge output was also utilized in the free vibration tests to determine the natural frequency of the harvester and its damping ratio. A  $60\text{-s}$  signal from the strain gauge was recorded during each of these tests. The signals were processed to identify peaks and their locations using neighborhood comparison and first derivative evaluation, followed by the calculation of the vibration periods,  $T_i = (t_i - t_{i-1})$ . The natural frequency of vibration was determined by taking the inverse of the average cycle period. In this study, the natural frequencies of the oscillators ranged from  $1.62$  to  $2.43 \text{ Hz}$ .

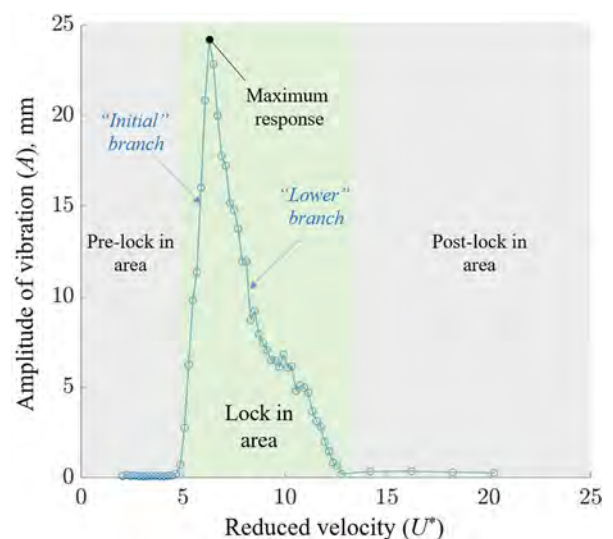


FIG. 2. Typical amplitude response of a vibrating cylinder (diameter of  $40$  and  $400 \text{ mm}$  long), with a  $15.75 \text{ N/m}$  stiffness beam, and a  $70 \text{ g}$  vibrating mass.

The same set of peaks was used to calculate the damping ratio of the oscillators using the logarithmic decrement method. The structural damping ratio varied from 0.12% to 0.19%, with an average of 0.15%.

The cylinders were 3D printed from polylactic acid (PLA) plastic, each was printed in two sections, which were then assembled into one piece. They are designed to be hollow inside with strengthening ribs, as illustrated in Fig. 5.

The experiments for this research were conducted in the large-scale atmospheric wind tunnel facility of the Mechanical Engineering Department at the City College of New York (CCNY). This open-ended suction-type wind tunnel has a test section of  $1.2 \times 1.2 \text{ m}^2$  cross section and 8.4 m long working area. It is powered by a 20 b.h.p. electric motor with fine speed control that provides up to 15 m/s free-stream velocity in the test section. The experimental setup was positioned 7 m downstream of the entrance of the test section (as shown in Fig. 6). All tests were performed within a Reynolds number range of 400–7500, covering the full range of vibration for all oscillator configurations. Transparent side walls and a top viewport allowed for the use of flow visualization equipment, including a high-speed camera and a continuous laser. The NOVA R3-4K high-speed camera, paired with Photron FASTCAM Viewer (PFV4) software, recorded images at a resolution of  $4096 \times 2304$  pixels at 250 frames per second. A DHOM-H-532-1000 laser provided strong laser illumination of 532 nm to capture vortex shedding, with beam intensity controlled by a DC power supply with an adjustable voltage output ranging from 0 to 5 V. Additionally, a Magnum 1200 fog generator, using JEM PRO-FOG fluid, produced dense vapor droplets for flow visualization. A DANTEC CTA hot-wire 56C17 probe, positioned 4 diameters downstream and 1.5 diameters to the side of the cylinder axis, was used to

measure airflow fluctuations due to vortex shedding at a scan rate of 1000 Hz.

In this study, cylinders with a height of 400 mm and three different diameters (20, 30, 40 mm) were employed. The cylinders were mounted on the double-beam support structure with three different beam lengths (i.e., 450, 498 and 546 mm). The cylinder masses were adjusted for each beam length, resulting in three total vibrating masses: 70, 80, and 90 g. The experiments covered independent variations of each parameter, resulting in a total of 27 harvester configurations.

For each experiment, the system's response to different airflow velocities was recorded. The range of airflow velocities, spanning from 0 to 2.0 m/s, adequately covered the vibration intervals for all parameter variations. The step size in airflow velocities was 0.02 m/s, with a 3-min interval given for the system to reach a steady state at each airflow velocity.

The cylinder diameters and airflow velocities mentioned above correspond to a Reynolds number range of 400–7500, chosen for its practical relevance in small-scale energy harvesting, such as in HVAC systems where typical airflow velocities are between 0 and 2 m/s, and restricted space could limit cylinders diameters to less than 40 mm. This Reynolds number range encompasses the transitional and early turbulent regimes, where vortex shedding is sufficiently strong to induce effective VIV.

#### IV. RESULTS AND DISCUSSION

The typical behavior of the harvester can be described as follows (refer to Fig. 2): there is no vibration at low airflow velocities, marking the pre-lock-in regime. In the lock-in-regime, vibration initiates with a small increase in airflow velocity. For example, in the case of a 40 mm cylinder, with 15.75 N/m stiffness beams, and a 70 g vibrating mass, the vibration starts at an airflow velocity of 0.49 m/s with an amplitude of 2.7 mm (initial branch). Vibration amplitude then reaches its maximum amplitude at 0.61 m/s, peaking at 24.1 mm.

Notably, the amplitude attains its maximum value (peak amplitude) within a very narrow range of airflow velocities. The further increase in airflow velocity beyond the maximum point results in a decrease in vibration amplitude. The amplitude reduction occurs over a wider range of airflow velocities (lower branch); for instance, the peak vibration was observed at 0.61 m/s with a 24.1 mm amplitude and finishes at 1.2 m/s (i.e., the end of the lock-in regime). In the post-lock-in-regime, the amplitude of vibration again becomes negligibly small.

##### A. Effects of the cylinder oscillator mass

Increasing the mass of the harvester, while keeping other parameters constant, leads to a reduction in the natural frequency of vibration. Consequently, as predicted by the constant Strouhal number for a stationary cylinder, resonance occurs at a lower airflow velocity compared to lighter cylinders, a hypothesis confirmed by the experimental results shown in Fig. 7.

Heavier cylinders initiate vibration slightly earlier than their lighter counterparts. The experiments revealed that, in terms of the Strouhal number, the vibration commenced (beginning of the lock-in regime) at  $St = 0.186\text{--}0.197$  for all three different masses. This result aligns with studies of stationary cylinders, which indicate  $St = 0.180\text{--}0.200$  for the wake vortex frequency. As expected, vibration initiates

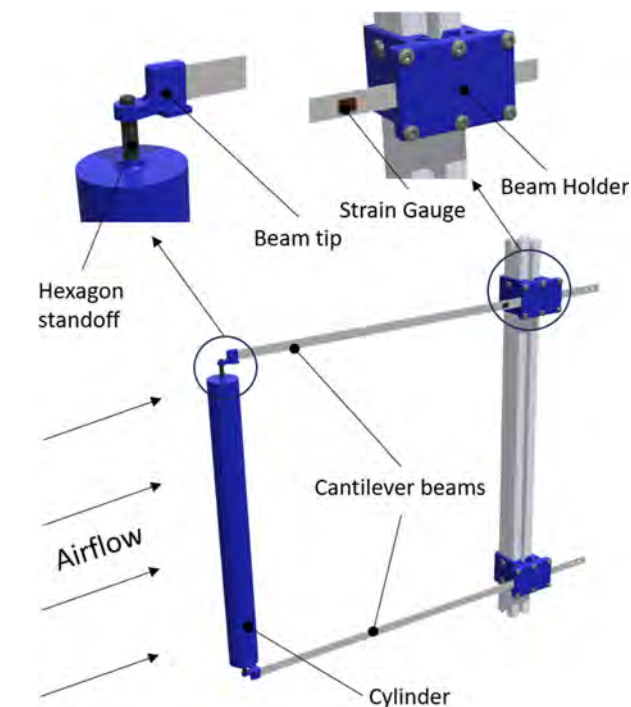


FIG. 3. Detailed design of the energy harvester model.

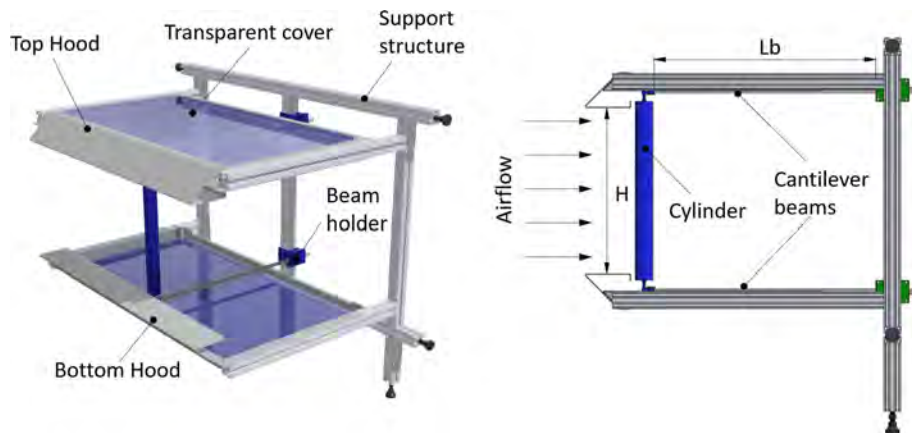


FIG. 4. The cylinder and beam mounting structures used in the present study.

when the vortex shedding frequency approaches the natural frequency of the system.

It was observed that mass change not only shifts the location of the peak amplitude but also affects its magnitude. For example, in the case of a 40 mm diameter cylinder on a 451 mm long beam, the peak amplitude of vibration decreased from 24.1 mm for a 70 g mass to 21.3 mm for a 90 g mass, as shown in Fig. 7. Figure 7(a) presents the amplitude of vibration as a function of airflow velocity, while Fig. 7(b) illustrates the same results using dimensionless parameters, with the amplitude ratio plotted against the reduced velocity.

The end of the lock-in regime for the 40 mm cylinder occurred at  $St = 0.080$ – $0.085$ . This consistent value of  $St$  introduces a significant difference in terms of the absolute value of the airflow velocity. The onset of the lock-in regime varies from 0.49 to 0.45 m/s for the 70 and 90 g harvesters, respectively. The end of the lock-in regime ranges from 1.20 to 1.00 m/s for the 70 and 90 g harvesters, respectively.

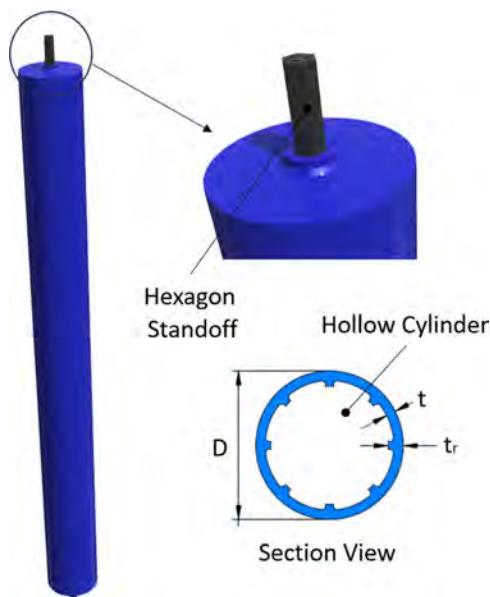


FIG. 5. Three-dimensional (3D) printed cylinder model with inner structural details.

Maintaining a constant  $St$  for the initiation and conclusion of the lock-in regime suggests that reducing the mass of the harvester will lead to a wider velocity window of the lock-in regime.

## B. Effects of the stiffness of the oscillator system

Changes in the system stiffness result in alterations to the natural frequency of the system. In this study, the variation in stiffness was achieved by adjusting the length of the beams and measured by the free-vibration testing described above. The impact of these stiffness changes is demonstrated in Fig. 8, which compares the results for a 40 mm diameter cylinder with a 70 g mass on three different beam lengths. Figure 8(a) shows the amplitude of vibration as a function of airflow velocity, while Fig. 8(b) depicts the same data in dimensionless terms, plotting the amplitude ratio against the reduced velocity. The peak amplitude increases and shifts to higher airflow velocities for the shorter (i.e., stiffer) beams, reflecting the increase in the natural frequency of the system.

For the 451 mm long beams with a 70 g mass, the natural frequency of the system was 2.43 Hz, whereas for the 546 mm long beams, it was 1.85 Hz. The system with 546 mm beams initiated vibration at 0.40 m/s and concluded at 0.92 m/s. In contrast, the system with 451 mm beams commenced vibration at 0.49 m/s and concluded at 1.20 m/s.

For all beam lengths, the onset of the lock-in regime occurred at  $St = 0.188$ – $0.197$ , and the end of the lock-in regime was observed at  $St = 0.080$ – $0.085$ . These  $St$  values remained relatively constant for different masses of the system, as discussed earlier. It appears that the natural frequency of the system influences the window of the lock-in regime, whereas the mass or stiffness of the system alone does not.

## C. Effects of the diameter of the cylinder oscillator

Figure 9 displays the outcomes of experiments conducted on three harvesters with varying cylinder diameters (i.e., 20, 30 and 40 mm), but identical in terms of stiffness and mass (i.e.,  $k = 15.75$  N/m and  $m_v = 70$  g). The experimental results highlight a significant variation in both the peak amplitude and the lock-in regime window for cylinders with different diameters.

The diameter of the cylinder appears to exert the most pronounced effect on vibration. For harvesters identical in stiffness, mass,



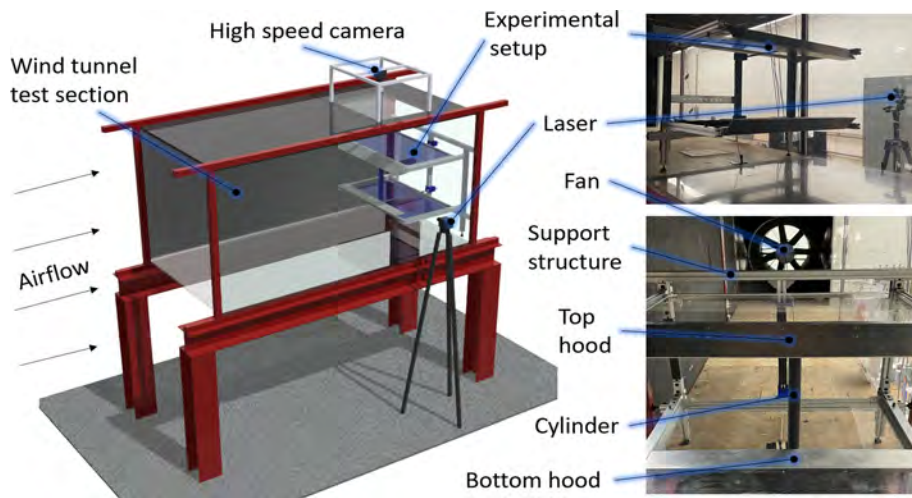


FIG. 6. Experimental setup in the wind tunnel test.

and natural frequency, a nearly fivefold change in peak amplitude is observed with just a twofold change in diameter.

Despite the diverse diameters, the initiation of the lock-in regime consistently follows  $St = 0.175$ – $0.197$ . However, the termination of the lock-in regime is found to be diameter-dependent and remains constant for each diameter (i.e., independent of mass and stiffness). The study revealed that the end of the lock-in regime occurred at  $St = 0.145$ – $0.155$  for a 20 mm cylinder,  $St = 0.125$ – $0.134$  for a 30 mm diameter, and  $St = 0.080$ – $0.085$  for a 40 mm diameter. Remarkably, these values remain consistent across various combinations of stiffness and masses in the system.

A key observation is that larger cylinder diameters lead to significantly higher vibration amplitudes and wider lock-in regime windows. As the beginning of the lock-in regime remains constant for any cylinder diameter, the end of lock-in shifts to higher airflow velocities. Furthermore, the diameter of the cylinder, by influencing the end of the lock-in window, becomes a determinant of the width of the lock-in regime. Details of these observations will be discussed in the following sections.

#### D. The peak amplitude of vibration

The peak amplitudes ( $A^*_{peak}$ ) of vibration for all cases are illustrated in Fig. 10. Based on these results, it is evident that an increase in the mass of the harvester leads to a nearly proportional decrease in the maximum amplitude of vibration. The variation in the stiffness of the system (beam length) also influences the maximum amplitude. As depicted in Fig. 10, stiffer systems exhibit higher peak amplitudes for all masses and diameters. The effect of system stiffness diminishes for smaller diameters of the cylinders, becoming nearly negligible in the case of a 20 mm diameter. Figure 10 illustrates that cylinder diameter has a large effect on vibration amplitude.

As previously mentioned, the mass ratio  $m^*$  has a significant effect on the vibrational behavior. For the case of a 70 g vibrating mass and 15.75 N/m stiff oscillators, the mass ratio is 113, 208, and 458 for cylinder diameters of 40, 30, and 20 mm, respectively. From the variation in mass ratio, we can draw the following conclusion: a higher mass ratio leads to a reduction in both the peak vibration amplitude and the vibration bandwidth.

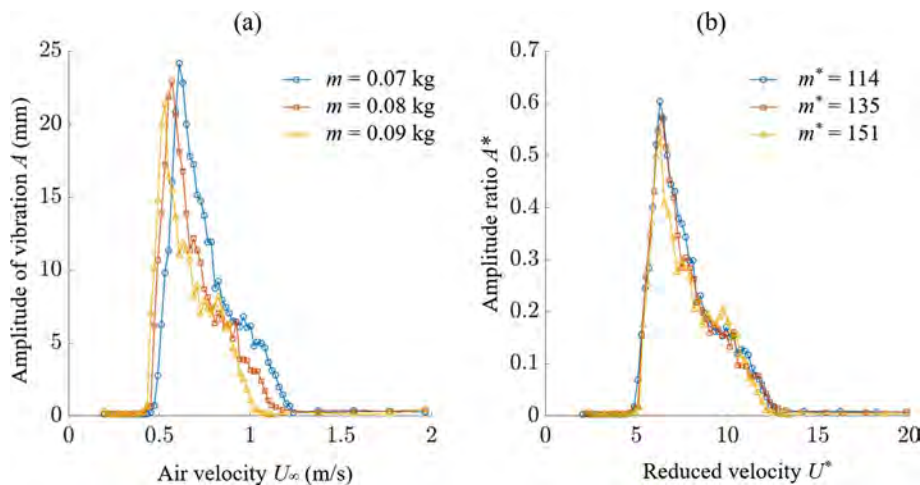
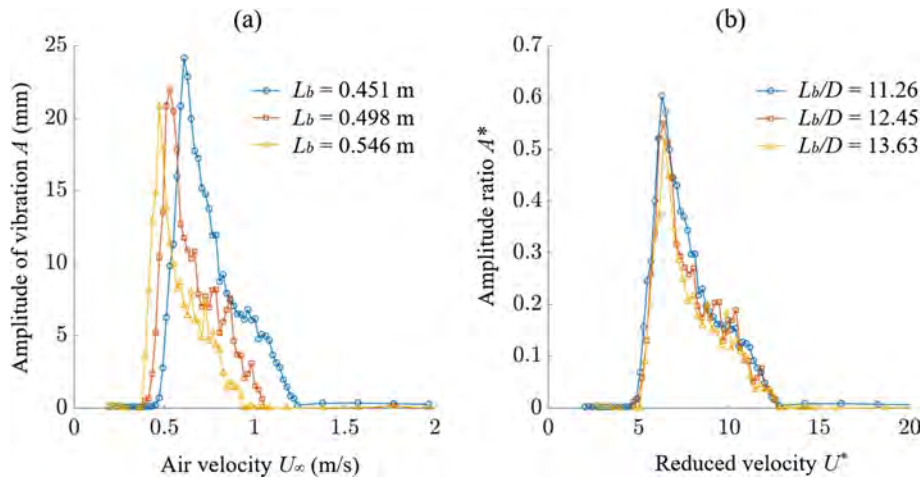


FIG. 7. Amplitude response of a 40 mm diameter cylinder on a 451 mm long beam with three different masses (mass ratio): (a) vibration amplitude (mm) vs air velocity (m/s) and (b) amplitude ratio ( $A^* = \frac{A}{D}$ ) vs reduced velocity ( $U^* = \frac{U_\infty}{f_n D}$ ).





**FIG. 8.** Amplitude response of a 40 mm diameter cylinder with 70 g vibrating mass on the 451, 498, and 546 mm long beams: (a) vibration amplitude (mm) vs air velocity (m/s) and (b) amplitude ratio  $A^*$  vs reduced velocity  $U^*$ .

A comparison of our results with experimental data from Ref. 44 is shown in Fig. 11, where the peak amplitude is plotted against the mass-damping parameter. The added mass is defined as  $m_a = C_A \rho \pi D^2 L / 4$ , where  $C_A$  represents the ideal added mass coefficient, which is equal to 1.0 for a circular cylinder oscillating transversely in an ideal, incompressible fluid.<sup>45</sup> As shown in the plot, there are three distinct groups of data points, each corresponding to a different oscillator diameter studied in the experiments. These groups appear because changing the cylinder diameter, while keeping mass constant, significantly affects the mass ratio i.e.,  $m^* = \frac{m_v}{\rho \pi D^2 L / 4}$ , even though the structural damping ratio i.e.,  $\zeta = \frac{c}{2\sqrt{m_v k}}$  remains nearly the same. The mass ratio of the oscillators across all configurations ranged from 113 to 603 (113–150 for a 40 mm diameter, 208–267 for a 30 mm diameter, and 458–603 for a 20 mm diameter) while the structural damping ratio varied from 0.12% to 0.19%, with an average of 0.15%. For instance, doubling the diameter results in a fourfold increase in mass ratio. Specifically, decreasing the cylinder diameter from 40 to 20 mm increases the mass ratio by approximately 300%. By contrast, the mass variation in our experiments was limited to around 30% across all tests. Additionally, while the stiffness of the system was adjusted by altering the length of the beams, this did not substantially

affect the mass ratio. The equivalent vibrating mass ( $m_v$ ) at the cylinder axis varied by only about 3 g with changes in beam length, which is minor compared to the total vibrating mass range of 70–90 g.

### E. Location of the lock-in interval

A summary of the lock-in interval in terms of Strouhal number for all cases can be seen in Fig. 12. The initiation of vibration (start of the lock-in regime) consistently occurred at  $St = 0.19$  on average across all 27 harvesters. This indicates a constant Strouhal number at the beginning of vibration. The peak amplitude was consistently reached at  $St = 0.161$  on average for all harvesters. This result suggests a constant Strouhal number at the point of peak amplitude. Note that the fluctuations in the  $St$  at lock-in start, especially for the smaller diameter ( $D = 20$  mm) cylinder, could be due to the difficulty in determining a consistent start of vibration for the relatively small amplitudes of the vibration.

In contrast, the conclusion of the lock-in regime varies with the diameter of the cylinders. Notably, the 40 mm diameter cylinder vibrates for over a wider range of flow velocities than the 30 and 20 mm cylinders across various combinations of stiffnesses and masses.

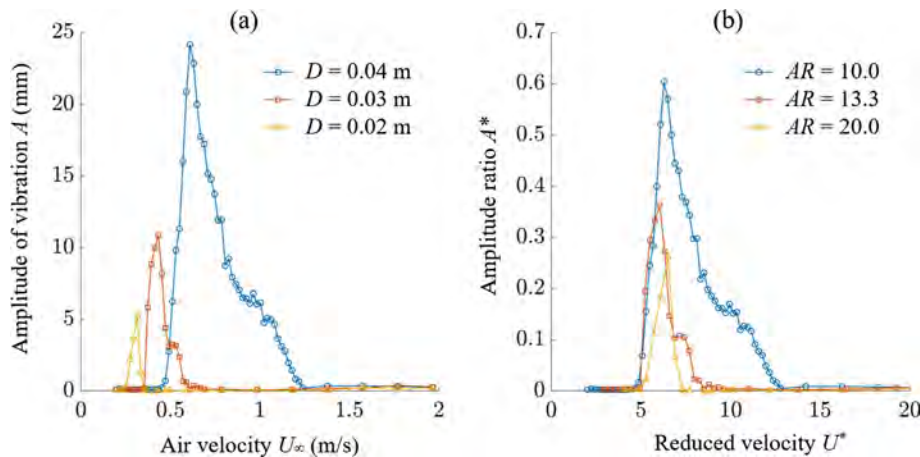


**FIG. 9.** Amplitude response of the oscillators on 451 mm long beams, with 70 g vibrating mass, and three different cylinder diameters: (a) vibration amplitude (mm) vs air velocity (m/s) and (b) amplitude ratio  $A^*$  vs reduced velocity  $U^*$ .

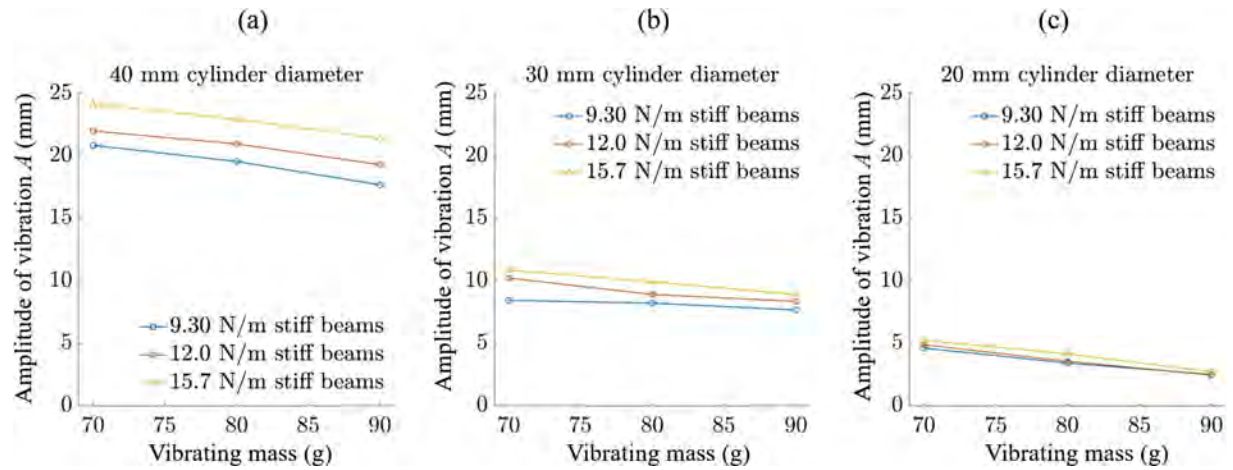


FIG. 10. Peak amplitude of the vibration as a function of vibrating mass and beam stiffness: (a) 40 mm cylinder diameter; (b) 30 mm cylinder diameter; and (c) 20 mm cylinder diameter.

Assuming a constant Strouhal number at the initiation and conclusion of vibration for a fixed-diameter harvester, we can derive the following relationship

$$\frac{\Delta U'}{\Delta U''} = \frac{U_2' - U_1'}{U_2'' - U_1''} = \frac{\frac{f_n' D}{St_2} - \frac{f_n' D}{St_1}}{\frac{f_n'' D}{St_2} - \frac{f_n'' D}{St_1}} = \frac{\frac{f_n'}{St_2} - \frac{f_n'}{St_1}}{\frac{f_n''}{St_2} - \frac{f_n''}{St_1}} \quad (1)$$

$$= \frac{f_n' \left( \frac{1}{St_2} - \frac{1}{St_1} \right)}{f_n'' \left( \frac{1}{St_2} - \frac{1}{St_1} \right)} = \frac{f_n'}{f_n''}, \quad (2)$$

$$\frac{\Delta U'}{\Delta U''} = \frac{f_n'}{f_n''}.$$

where  $\Delta U'$ —bandwidth of the harvester with natural frequency of vibration  $f_n'$ ,  $\Delta U''$ —bandwidth of the harvester with natural frequency of vibration  $f_n''$ ,  $U_1$ —free stream velocity at initiation of vibration,  $U_2$ —free stream velocity at conclusion of vibration,  $St_1$ —Strouhal number at the initiation of vibration, and  $St_2$ —Strouhal number at the conclusion of vibration.

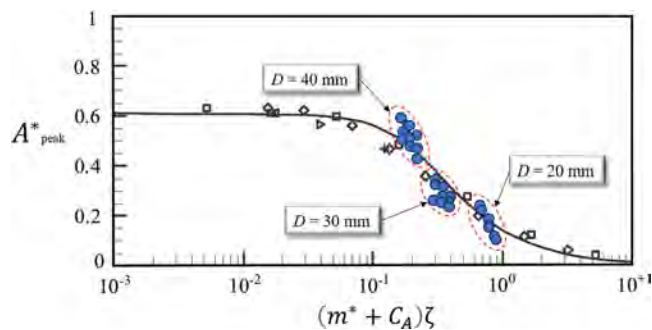


FIG. 11. Peak amplitude of the vibration vs a collection of the experimental data in Ref. 44.

The dependence of the lock-in interval on the natural frequency of the system is shown in Fig. 13(a). As illustrated, for oscillators with a 40 mm diameter cylinder, the initiation of vibration follows a nearly constant Strouhal number at  $St = 0.186$  (linear fit). A similar pattern is observed at the conclusion of vibration, which also follows a nearly constant Strouhal number, but at a different value of  $St = 0.081$  (linear fit). The slopes of the solid lines in the plot represent these Strouhal numbers. As the amplitude of vibration increases, the distance between the initiation and conclusion lines widens, resulting in a broader vibration bandwidth.

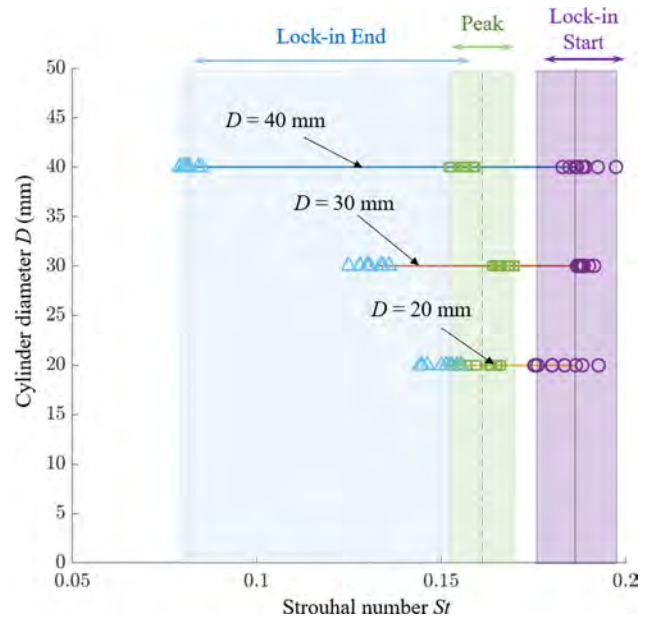


FIG. 12. The positions of the initiation, peak, and conclusion of vibration for harvesters with varying diameters.

Figure 13(b) presents the collection of all 27 oscillators, illustrating the relationship between each oscillator's natural frequency and its vibration bandwidth for each cylinder diameter studied. The plot shows that an increase in natural frequency leads to a corresponding increase in vibration bandwidth. Additionally, the slope of the approximation (solid) line decreases with increasing cylinder diameter, suggesting that larger cylinders tend to exhibit a broader lock-in interval.

This result demonstrates that changes in the natural frequency of the harvester lead to proportional changes in vibration bandwidth. This outcome aligns with the effect of mass ratio,<sup>4</sup> as increasing the natural frequency of a cylinder oscillator is achieved by reducing the vibrating mass, thereby lowering the mass ratio. Figure 14 illustrates the effect of mass ratio on the initiation and conclusion of vibration for the 27 oscillator configurations. The initiation of vibration appears largely independent of the mass ratio, occurring at a reduced velocity of approximately 5.2–5.4. In contrast, the conclusion of vibration shifts to significantly higher velocities as the mass ratio decreases, indicating a substantial increase in the bandwidth of vibration with lower mass ratios. The plot includes least squares fits for the effect of mass ratio on the reduced velocities at the initiation and conclusion of vibration. Additionally, when the natural frequency is altered by adjusting the beam length, corresponding changes in bandwidth are observed. Oscillators with identical mass and cylinder diameter display a wider vibration bandwidth at higher natural frequencies, achieved by using shorter beams.

Consequently, harvesters with a higher natural frequency will exhibit a wider range of airflow velocities over which they vibrate (i.e., a larger lock-in region), with the lock-in occurring at higher airflow velocities.

## F. Flow visualization and analysis of cylinder wake

The wake flow structure was captured using a high-speed camera in combination with a continuous laser illumination and fog tracer system. This setup captured the flow structure for the oscillator

configuration with the highest amplitude response: a 40 mm diameter, 70 g vibrating mass, and 15.75 N/m stiffness, resulting in a natural frequency of 2.43 Hz. A hot wire anemometer was located downstream of the cylinder to capture velocity fluctuation frequencies, predominantly caused by vortex shedding from the cylinder surface.

The experiment spanned the entire vibration bandwidth, with a focus on key points of interest: the initial branch (low amplitude), initial branch (high amplitude), peak amplitude, lower branch (high amplitude), and lower branch (low amplitude), as shown in Fig. 15.

No vortex formation was observed in the wake close to the cylinder surface (i.e., within  $X/D = 1.5$ ) during the pre-lock-in regime. This result was confirmed by the hot-wire readings [Fig. 16(a)]. It is suggested that when the airflow velocity is low, the cylinder with a finite length may not be able to trigger the rolling up of shear layers, disrupting the formation of classical Karman vortex street structure in the wake flow.<sup>2</sup> However, even without a dominant frequency in the wake, the system enters resonance at a Strouhal number of 0.19, marking the beginning of the lock-in regime, where the frequency of vortex shedding matches the natural frequency of the system [Figs. 16(b) and 16(c)].

After the onset of the lock-in regime, a further increase in airflow velocity leads to a sharp rise in the amplitude response. At this point, a single vortex is shed from the cylinder surface during each half-cycle of the vibration. As the system approaches the peak of vibration, more intense vortex formation occurs closer to the cylinder surface.

At the peak of vibration, the formation of vortex pairs becomes clearly visible, occurring every half-cycle. This phenomenon takes place very close to the downstream surface of the cylinder, which can create the most significant pressure fluctuations and result in the peak vibration response.

After reaching peak vibration, further increases in airflow velocity lead to a reduction in amplitude response. As shown in Fig. 15, the vortex pairs shift further downstream. As airflow velocity continues to increase in the lower branch, the vortex formation moves even further

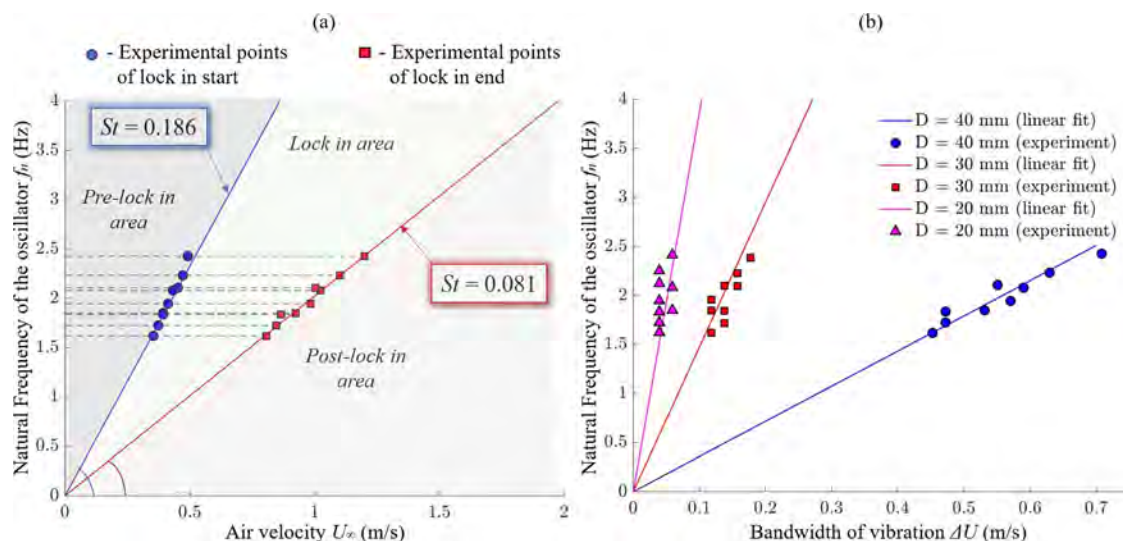


**FIG. 13.** The lock-in interval: (a) vibration initiation and conclusion as a function of natural frequency of the systems for the 40 mm diameter cylinder and (b) vibration bandwidth for all studied oscillators.



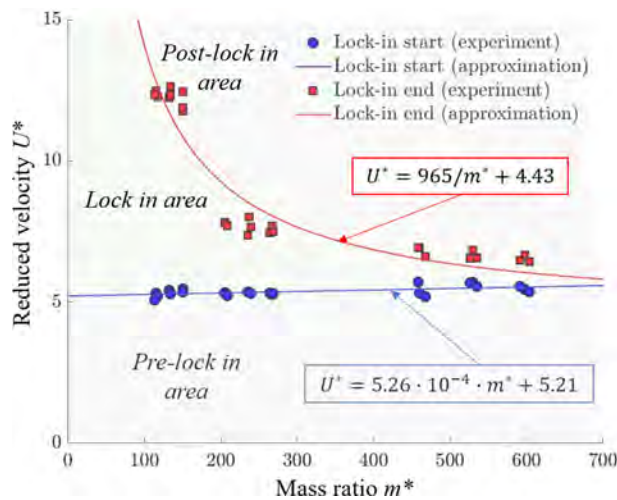


FIG. 14. Effect of the mass ratio  $m^*$  on the initiation and conclusion of the cylinder vibration.

downstream. As a result, the pressure variations on the cylinder surface associated with the wake vortices become less significant, reducing the fluctuating side forces that drive the vibrations.

As the system exits the lock-in region, a weak peak frequency at 5.8 Hz was observed in the downstream wake [Fig. 16(d)], corresponding to a Strouhal number of 0.15. This result aligns with the data presented in Ref. 38 for finite-length stationary cylinders.

With an increase in vibration amplitude, the kinematics of the oscillator in the crossflow direction also changes, while the frequency of vibration remains constant, equal to the natural frequency of the system. The vibrational motions of the oscillator generate an induced velocity, i.e.,  $U_o$ , which fundamentally alters the effective incoming flow directions (the angle  $\alpha$  between the freestream velocity and the absolute velocity) as well as the airflow velocity magnitude [Fig. 17(a)]. As the amplitude grows, the cylinder's wake increasingly rotates around the cylinder axis, exposing it more to the ambient flow.

In the case of peak vibration for the oscillator with the highest amplitude in the experiments, the freestream velocity was 0.61 m/s, with a vibration amplitude of 24 mm. This oscillator had a natural frequency of 2.43 Hz, resulting in a maximum velocity (at the midpoint of its motion) of 0.37 m/s, which is comparable to the freestream velocity. The angle  $\alpha$  reached a maximum of  $31^\circ$  at this midpoint velocity and decreased to zero as the oscillator moved toward its limiting position, where the velocity dropped to zero.

Two distinct vortex-shedding patterns are observed in the wake of a vibrating cylinder. In the “2S” regime, each cycle of cylinder motion generates two single vortices on alternating sides, forming a classic Kármán vortex street. In contrast, the “2P” regime involves the formation of two pairs of vortices per cycle, with each half-cycle producing a pair of vortices on either side of the cylinder. These regimes represent different modes of vortex shedding, influenced by flow parameters and the vibration characteristics of the cylinder.<sup>4</sup> Both regimes were observed in the current research: the “2S” regime appeared in the initial branch of the cylinder's oscillation until the amplitude reached  $A^* = 0.4$ . Beyond this amplitude, the system shifted to the “2P” vortex formation regime, which persisted until the end of

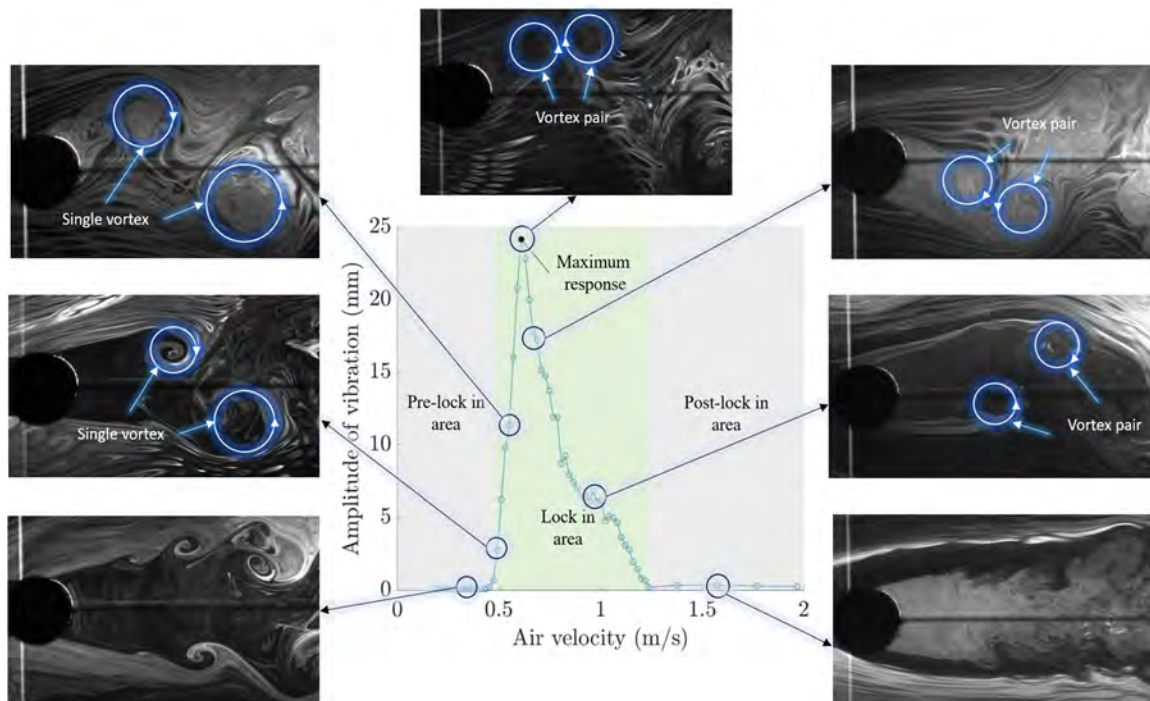
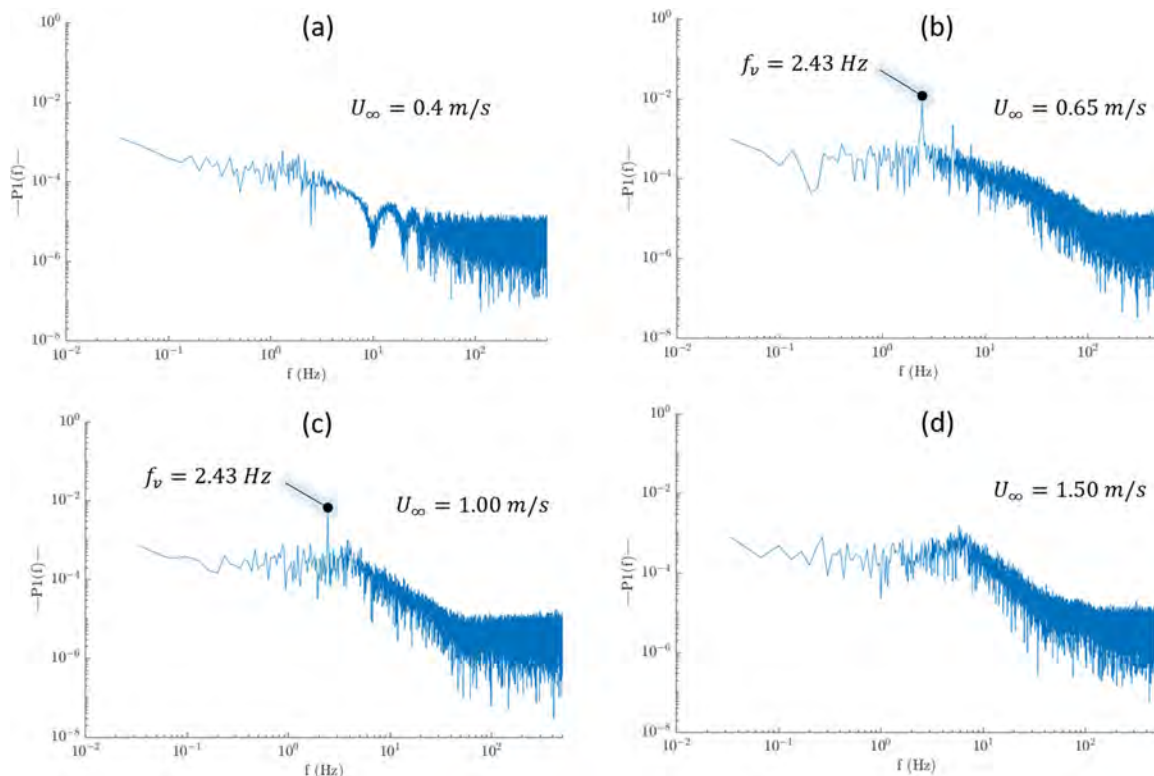


FIG. 15. Visualization of the flow behind the cylinder oscillator at different air velocities (40 mm diameter cylinder, 70 g vibrating mass, and 15.75 N/m stiffness).





**FIG. 16.** Frequency spectrum from the hot wire, located four diameters downstream and one diameter to the side of the cylinder (40 mm diameter cylinder, 70 g vibrating mass, and 15.75 N/m stiffness).

the lock-in region. In the post-lock-in region, no evident vortex structures were observed within a distance of approximately six cylinder diameters downstream.

Based on high-speed camera recordings of the wake, a hypothesis was developed to explain this wake behavior, which requires further validation through particle image velocimetry (PIV) measurements.

As the cylinder begins to vibrate, its dynamic motions significantly increase the likelihood of shear layer roll-up. For instance, as the cylinder moves upward from its lowest point during

vibration [Fig. 17(b)], the shear layer previously formed on the cylinder's lower surface is intensified by the more energetic incoming flow (due to the fleeing of the cylinder), inducing the formation of a pair of vortices in the wake flow [Fig. 17(b)]. At moderate amplitudes, where the cylinder's velocity and angle  $\alpha$  are relatively small, only one vortex becomes exposed to the ambient flow when the cylinder changes its direction of motion. This exposed vortex, on the side opposite to the cylinder's movement (the outside vortex), sheds from the cylinder surface, while the other vortex (the inside

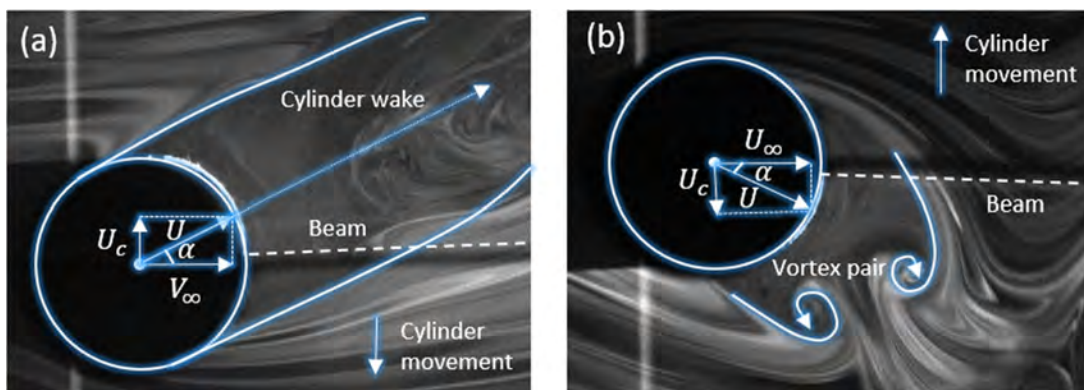


**FIG. 17.** Smoke visualization of the cylinder wake: (a) cylinder wake orientation and (b) vortex pair in the cylinder wake.

vortex) remains hidden by the cylinder body. This configuration results in the “2S vortex” mode.

As the amplitude increases further,  $\alpha$  increases (up to  $31^\circ$  in the current research), and both vortices become exposed to the ambient flow when the cylinder changes its direction of motion, allowing a pair of vortices to shed from the cylinder surface, marking the transition to the “2P vortex” mode. This mode results in larger vibrations due to greater net energy input, and with further increases in airflow velocity, it drives the system to peak vibration.

As the airflow velocity continues to rise, the formation of vortex pairs progressively shifts downstream. This downstream movement likely reduces pressure fluctuations on the cylinder surface, leading to a decrease in net energy input per vibration cycle. This behavior explains why increased air velocities eventually lead to a reduction in vibration amplitude, marking the end of the lock-in interval. At this stage, the vortex-shedding frequency falls out of sync with the natural frequency of the system, leading to a loss of resonance, and further increases in airflow velocity no longer sustain significant vibrations.

### G. Oscillator energy conversion

To estimate the energy generated by vortex-induced vibrations (VIV) of the cylinder, we model the vibrating system as a single degree-of-freedom oscillator coupled with a piezoelectric generator.<sup>11</sup> Though a number of energy generation circuits have been proposed in the literature,<sup>46</sup> estimates for generated electrical power are often calculated assuming a purely resistive electric load resistance  $R$ .<sup>11,47</sup> When Kirchhoff's current law (KCL) is applied to the piezoelectric energy harvester, the derived load voltage is given by

$$\theta \frac{dy}{dt} + C_p \frac{dv_L}{dt} + \frac{v_L}{R} = 0. \quad (3)$$

Here,  $\theta$  is the electromechanical coupling parameter,  $y$  is the tip displacement,  $C_p$  is the piezo capacitance, and  $v_L$  is the load voltage.

By applying the Fourier transform to (3) and solving for the load voltage magnitude ( $V_L$ ), we obtain

$$V_L = \frac{\omega \theta A R}{\sqrt{(\omega C_p R)^2 + 1}}. \quad (4)$$

Here, the tip displacement  $y$  is assumed to be harmonic with amplitude  $A$ . The magnitude of the electrical power delivered to the load is given by the equation

$$P = \frac{V_L^2}{R} = \frac{(\omega \theta A)^2 R}{(\omega C_p R)^2 + 1}. \quad (5)$$

Assuming a weakly electromechanically coupled system, optimal power transfer occurs when<sup>47</sup>

$$R_{opt} = \frac{1}{\omega C_p}. \quad (6)$$

By substituting  $R_{opt}$  into the power equation, we derive

$$P_{opt} = \frac{V_{L_{opt}}^2}{R_{opt}} = \frac{\omega \theta^2 A^2}{2 C_p}. \quad (7)$$

The optimal non-dimensional power can then be expressed as

$$P_{opt}^* = P_{opt} \frac{C_p}{\omega_n \theta^2 D^2} = \frac{1}{2} \left( \frac{A}{D} \right)^2 \left( \frac{\omega}{\omega_n} \right). \quad (8)$$

In the lock-in regime, the system vibrates at its natural frequency (resonance condition), so  $\frac{\omega}{\omega_n} = 1$ , and Eq. (8) simplifies to

$$P_{opt}^* = \frac{1}{2} \left( \frac{A}{D} \right)^2. \quad (9)$$

Equation (9) shows that the optimal power output is proportional to the square of the amplitude ratio. Using this relationship, the dimensionless power corresponding to the peak amplitude cases for all 27 energy harvester configurations was plotted against the mass ratio (see Fig. 18).

As shown in Fig. 18, the power output decreases significantly as the mass ratio increases. This trend arises because the mass ratio affects the peak amplitude of vibration, and the squaring of the amplitude ratio in the power output equation further amplifies the effect. These findings underscore the importance of maximizing the oscillator's vibration amplitude in energy harvesting applications.

As an example of power output of the harvester, we utilize a harvester configuration similar to the one investigated in Ref. 11, where a piezoelectric element is bonded to the face of the beam near the clamped end.

We consider the case of the maximum vibration amplitude observed in this study (cylinder diameter: 40 mm, beam length: 450 mm, vibrating mass: 70 g), where the peak amplitude reached 24.1 mm.

To estimate the power output, a piezoelectric patch made of PZT-5A is investigated with the following parameters: length  $l_p = 31.8$  mm, width  $h_p = 25.4$  mm, thickness  $t_p = 0.267$  mm, and Young's modulus  $Y_p = 66$  GPa. The patch is bonded at a distance of  $l_0 = 2$  mm from the fixed end of the beam. The capacitance of the patch is given by

$$C_p = \frac{k_{33}^- h_p l_p}{t_p}, \quad (10)$$

where  $k_{33}^- = 13.28$  nF/m is the permittivity of the piezoelectric under constant strain.<sup>11</sup>

The piezoelectric current  $i_p$ , which is related to the trip deformation, is then expressed as<sup>11</sup>

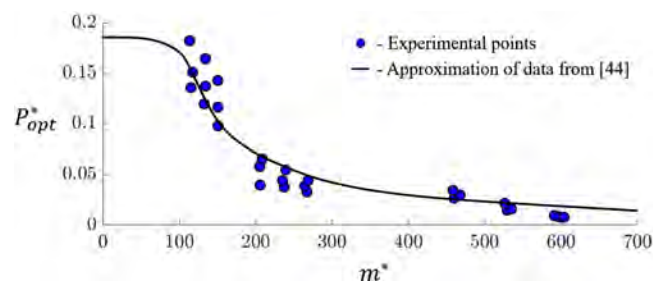


**FIG. 18.** Dimensionless power output at peak amplitude vs mass ratio: full circles—experimental values of the peak amplitude for the 27 energy harvester configurations, solid line—approximation of data from Ref. 44.

$$i_p = \theta \dot{y} = -d_{31} Y_p h_p \frac{\partial}{\partial t} \left( \int_{s=l_0}^{l_0+l_p} \varepsilon_p(s, t) ds \right), \quad (11)$$

where  $d_{31} = -190 \text{ pm/V}$  is piezoelectric constant,  $\varepsilon_p(s, t) = \frac{3y(L_b-s)(h_b-h_p)}{2L_b^3}$  is the strain at the mid-height of the piezoelectric patch. Throughout this derivation, the presence of the piezoelectric patch is assumed not to contribute any meaningful stiffness or damping to the system and thus does not affect the maximum displacement or resonant frequency of the harvester.

By substituting the strain expression for a cantilever beam at the location of the piezoelectric patch, the electromechanical coupling coefficient  $\theta$  is obtained as

$$\theta = -d_{31} Y_p h_p \frac{3(t_b + t_p)}{2L_b^3} \left[ L_b l_p - \frac{(l_0 + l_p)^2}{2} + \frac{l_0^2}{2} \right]. \quad (12)$$

The optimal power output is determined by substituting  $C_p$ ,  $\theta$ ,  $A$ , and  $\omega$  (equal to  $\omega_n$  in the lock-in regime) into Eq. (7). For the maximum vibration amplitude observed in this study, the optimal power output was found to be 1.8 mW. Note that the harvested power can be increased by attaching additional piezoelectric patches to the beams.

## V. CONCLUSIONS

This paper investigated the critical parameters influencing a vortex-induced vibration (VIV) energy harvester and provided insights into the complex wake dynamics associated with the oscillator's amplitude response. A systematic experimental study was conducted to evaluate the effects of bluff body dimensions, vibrational stiffness, and mass on the vibration behaviors of the VIV energy harvester system. In addition, high-speed flow visualization is also conducted to elucidate the transition of wake modes and the resulting impact on vibration amplitude, which directly governs the energy harvesting through the system.

The experimental results confirmed classical VIV behavior, characterized by distinct pre-lock-in, lock-in, and post-lock-in stages. It was observed that the peak vibration amplitude, a key determinant of the energy output, is highly sensitive to changes in model parameters. Specifically, an increase in the vibrating mass led to a reduction in the peak amplitude and shifted its occurrence to lower airflow velocities. Conversely, a reduction in mass not only increased the peak amplitude but also widened the lock-in window, allowing energy harvesting over a broader range of flow conditions. Additionally, the systems with increased stiffness or lower mass reached peak amplitudes at higher flow velocities, as predicted by Strouhal number considerations, with stiffer systems generally exhibiting larger amplitudes.

Cylinder diameter was found to significantly influence both the peak amplitude and the width of the lock-in regime. The cylinder oscillators with larger diameters produced higher peak amplitudes and broader lock-in ranges. Notably, the initiation of lock-in occurred consistently at Strouhal numbers between 0.175 and 0.197, while the termination was diameter-dependent—occurring at lower Strouhal numbers for larger cylinders. These findings indicate that both the natural frequency (affected by mass and beam length) and the cylinder diameter are critical in tuning the vibration bandwidth and optimizing energy harvesting performance.

High-speed flow visualization and hot-wire anemometry further revealed that vortex shedding dynamics change with airflow velocity. In the lock-in regime, a sharp increase in vibration amplitude was accompanied by the shedding of a single vortex per half-cycle at moderate amplitudes and the formation of vortex pairs at peak amplitudes, which likely enhanced pressure fluctuations. Beyond the peak, vortex shedding shifted downstream, diminishing the pressure fluctuations in the cylinder's boundary layer and, consequently, reducing the vibration amplitude.

The power output analysis demonstrates that the energy generated by the VIV harvester, when coupled with a piezoelectric generator, is critically dependent on the oscillator's vibration amplitude. The optimal, non-dimensional power output is proportional to the square of the amplitude ratio, indicating that reducing the mass ratio—which increases the vibration amplitude—significantly boosts harvested power. This study demonstrated that the proposed piezoelectric energy harvesting system achieves an optimal power output of 1.8 mW at maximum vibration amplitude which should be sufficient to power small-scale electronic devices. These findings provide a robust foundation for future research aimed at further optimizing VIV energy harvesters.

## ACKNOWLEDGMENTS

The research work is supported by the National Science Foundation (NSF) Award #2131600 and the Professional Staff Congress-City University of New York (PSC-CUNY) Enhanced Award.

## AUTHOR DECLARATIONS

### Conflict of Interest

The authors have no conflicts to disclose.

## Author Contributions

**Andrei Fershalov:** Data curation (lead); Formal analysis (lead); Methodology (equal); Visualization (equal); Writing – original draft (lead). **Niell Elvin:** Conceptualization (equal); Formal analysis (equal); Funding acquisition (equal); Investigation (equal); Methodology (equal); Project administration (equal); Supervision (equal); Visualization (equal); Writing – review & editing (equal). **Pieter Orlandini:** Data curation (equal); Methodology (equal); Visualization (equal). **Ilya Avros:** Data curation (equal); Formal analysis (equal); Investigation (equal); Methodology (equal). **Yang Liu:** Conceptualization (equal); Formal analysis (equal); Funding acquisition (equal); Investigation (equal); Methodology (equal); Supervision (equal); Visualization (equal); Writing – review & editing (equal).

## DATA AVAILABILITY

The data that support the findings of this study are available from the corresponding author upon reasonable request.

## REFERENCES

- J. H. Lienhard, "Synopsis of lift, drag, and vortex frequency data for rigid circular cylinders," Technical Report No. 300 (Washington State University, College of Engineering Research Division, Pullman, WA, 1966).



- <sup>2</sup>P. W. Bearman, "Vortex shedding from oscillating bluff bodies," *Annu. Rev. Fluid Mech.* **16**, 195–222 (1984).
- <sup>3</sup>T. Sarpkaya, "A critical review of the intrinsic nature of vortex-induced vibrations," *J. Fluids Struct.* **19**(4), 389–447 (2004).
- <sup>4</sup>C. H. K. Williamson and R. Govardhan, "Vortex-induced vibrations," *Annu. Rev. Fluid Mech.* **36**, 413–455 (2004).
- <sup>5</sup>D. Pastrana, I. Rodriguez, J. C. Cajas, O. Lehmkuhl, and G. Houzeaux, "On the formation of Taylor-Görtler structures in the vortex induced vibration phenomenon," *Int. J. Heat Fluid Flow* **83**, 108573 (2020).
- <sup>6</sup>R. D. Gabbai and H. Benaroya, "A first-principles derivation procedure for wake-body models in vortex-induced vibration: Proof-of-concept," *J. Sound Vib.* **312**(1–2), 19–38 (2008).
- <sup>7</sup>M. S. Aswathy and S. Sarkar, "Frequency characteristics and phase dynamics of a stochastic vortex induced vibration system," *J. Sound Vib.* **509**, 116230 (2021).
- <sup>8</sup>M. Raissi, Z. Wang, M. S. Triantafyllou, and G. E. Karniadakis, "Deep learning of vortex-induced vibrations," *J. Fluid Mech.* **861**, 119–137 (2019).
- <sup>9</sup>Y. Tamura, "Mathematical models for understanding phenomena: Vortex-induced vibrations," *Jpn. Archit. Rev.* **3**(4), 398–422 (2020).
- <sup>10</sup>L. Zhang, A. Abdelkefi, H. Dai, R. Naseer, and L. Wang, "Design and experimental analysis of broadband energy harvesting from vortex-induced vibrations," *J. Sound Vib.* **408**, 210–219 (2017).
- <sup>11</sup>H. D. Akaydin, N. G. Elvin, and Y. Andreopoulos, "The performance of a self-excited fluidic energy harvester," *Smart Mater. Struct.* **21**(2), 025007 (2012).
- <sup>12</sup>V. Azadeh-Ranjbar, N. G. Elvin, and Y. Andreopoulos, "Vortex-induced vibration of finite-length circular cylinders with spanwise free-ends: Broadening the lock-in envelope," *Phys. Fluids* **30**, 105104 (2018).
- <sup>13</sup>Z. Lai, S. Wang, L. Zhu, G. Zhang, J. Wang, K. Yang, and D. Yurchenko, "A hybrid piezo-dielectric wind energy harvester for high-performance vortex-induced vibration energy harvesting," *Mech. Syst. Signal Process.* **150**, 107212 (2021).
- <sup>14</sup>A. Erturk and D. J. Inman, *Piezoelectric Energy Harvesting* (John Wiley & Sons, New York, NY, 2011).
- <sup>15</sup>S. Roundy and P. K. Wright, "A piezoelectric vibration-based generator for wireless electronics," *Smart Mater. Struct.* **13**(5), 1131–1142 (2004).
- <sup>16</sup>J. J. Allen and A. J. Smits, "Energy harvesting EEL," *J. Fluids Struct.* **15**(5), 629–640 (2001).
- <sup>17</sup>G. W. Taylor, J. R. Burns, S. M. Kammann, W. B. Powers, and T. R. Welsh, "The energy harvesting EEL: A small subsurface ocean/river power generator," *IEEE J. Oceanic Eng.* **26**(4), 539–547 (2001).
- <sup>18</sup>W. Yang, J. Peng, Q. Chen, and S. Zhao, "Advancements and future prospects in ocean wave energy harvesting technology based on micro-energy technology," *Micromachines* **15**(10), 1199 (2024).
- <sup>19</sup>S. R. Anton and H. A. Sodano, "A review of power harvesting using piezoelectric materials (2003–2006)," *Smart Mater. Struct.* **16**(3), R1 (2007).
- <sup>20</sup>H. D. Akaydin, N. G. Elvin, and Y. Andreopoulos, "Wake of a cylinder: A paradigm for energy harvesting with piezoelectric materials," *Exp. Fluids* **49**(2), 291–304 (2010).
- <sup>21</sup>H. D. Akaydin, N. Elvin, and Y. Andreopoulos, "Energy harvesting from highly unsteady fluid flows using piezoelectric materials," *J. Intell. Mater. Syst. Struct.* **21**(13), 1263–1278 (2010).
- <sup>22</sup>O. Goushcha, H. D. Akaydin, N. Elvin, and Y. Andreopoulos, "Energy harvesting prospects in turbulent boundary layers," *J. Fluids Struct.* **54**, 823–847 (2015).
- <sup>23</sup>F. Pan, Z. Xu, P. Pan, and L. Jin, "Piezoelectric energy harvesting from vortex-induced vibration using a modified circular cylinder," in *Proceedings of the 20th International Conference on Electrical Machines and Systems (ICEMS), Sydney, NSW, Australia, 11–14 August 2017* (IEEE, 2017).
- <sup>24</sup>M. Verma and A. De, "Dynamics of vortex-induced vibrations of a slit-offset circular cylinder for energy harvesting at low Reynolds number," *Phys. Fluids* **34**, 083607 (2022).
- <sup>25</sup>U. Javed and A. Abdelkefi, "Characteristics and comparative analysis of piezoelectric-electromagnetic energy harvesters from vortex-induced oscillations," *Nonlinear Dyn.* **95**, 3309–1950 (2019).
- <sup>26</sup>I. Patrick, S. Adhikari, and M. I. Hussein, "Metaharvesting: Emergent energy harvesting by piezoelectric metamaterials," *Proc. R. Soc. A* **480**, 20240033 (2024).
- <sup>27</sup>D. Cao, X. Guo, J. Wang, and S. K. Lai, "Recent advancement of flow-induced piezoelectric vibration energy harvesting techniques: Principles, structures, and nonlinear designs," *Appl. Math. Mech. Engl. Ed.* **43**, 959–1472 (2022).
- <sup>28</sup>S. Bakhtiar, F. Khan, A. Z. Hajjaj, and H. Fu, "Fluid flow-based vibration energy harvesters: A critical review of state-of-the-art technologies," *Appl. Sci.* **14**, 11452 (2024).
- <sup>29</sup>P. Han, Q. Huang, G. Pan, D. Qin, W. Wang, R. T. Goncalves, and J. Zhao, "Optimal energy harvesting efficiency from vortex-induced vibration of a circular cylinder," *Ocean Eng.* **282**, 114869 (2023).
- <sup>30</sup>M. Zhang and J. Wang, "Experimental study on piezoelectric energy harvesting from vortex-induced vibrations and wake-induced vibrations," *J. Sens.* **2016**(2), 1–7.
- <sup>31</sup>M. Zhang, C. Zhang, A. Abdelkefi, H. Yu, O. Gaidai, X. Qin, H. Zhu, and J. Wang, "Piezoelectric energy harvesting from vortex-induced vibration of a circular cylinder: Effect of Reynolds number," *Ocean Eng.* **235**, 109378 (2021).
- <sup>32</sup>G. Hu, K. C. S. Kwok, K. T. Tse, and J. Song, "Aerodynamic modification to a circular cylinder to enhance the piezoelectric wind energy harvesting," *Appl. Phys. Lett.* **109**(19), 193902 (2016).
- <sup>33</sup>C. Xia, L. Tang, P. Yin, and K. C. Aw, "Multi-directional and multi-modal vortex-induced vibrations for wind energy harvesting," *Appl. Phys. Lett.* **125**(20), 203901 (2024).
- <sup>34</sup>A. Khalak and C. H. K. Williamson, "Dynamics of a hydroelastic cylinder with very low mass and damping," *J. Fluids Struct.* **10**, 455–472 (1996).
- <sup>35</sup>A. Khalak and C. H. K. Williamson, "Investigation of the relative effects of mass and damping in vortex-induced vibration of a circular cylinder," *J. Wind Eng. Ind. Aerodyn.* **69–71**, 341–350 (1997).
- <sup>36</sup>A. Khalak and C. H. K. Williamson, "Motions, forces and mode transitions in vortex induced vibrations at low mass-damping," *J. Fluids Struct.* **13**, 813–851 (1999).
- <sup>37</sup>T. Shepard, D. Law, J. Dahl, R. Reichstadt, and A. S. Selvamani, "Impact of aspect ratio on drag and flow structure for cylinders with two free ends," *J. Fluids Eng.* **145**, 091301 (2023).
- <sup>38</sup>D. A. Potts, J. R. Binns, H. Marcollo, and A. E. Potts, "The effect of aspect ratio on the drag of bare cylinders," in *Proceedings of the ASME 38th International Conference on Ocean, Offshore and Arctic Engineering (OMAE2019)*, Glasgow, Scotland, 9–14 June 2019, 2019.
- <sup>39</sup>T. Kitagawa, Y. Fujino, and K. Kimura, "Effects of free-end condition on end-cell-induced vibration," *J. Fluids Struct.* **13**(4), 499–518 (1999).
- <sup>40</sup>R. D. Blevins, *Flow-Induced Vibration* (Krieger Publishing Company, Waltham, MA, 2001).
- <sup>41</sup>C. Feng, "The measurement of vortex induced effects in flow past stationary and oscillating circular and D-section cylinders," Ph.D. dissertation (University British Columbia, Vancouver, Canada, 1968).
- <sup>42</sup>M. P. Paidoussis, S. P. Price, and E. de Langre, *Fluid-Structure Interactions: Cross-Flow-Induced Instabilities* (Cambridge University Press, Cambridge, UK, 2010).
- <sup>43</sup>Y. Liao and H. A. Sodano, "Optimal parameters and power characteristics of piezoelectric energy harvesters with an RC circuit," *Smart Mater. Struct.* **18**(4), 045011 (2009).
- <sup>44</sup>P. Anagnostopoulos and P. W. Bearman, "Response characteristics of a vortex-excited cylinder at low Reynolds numbers," *J. Fluids Struct.* **6**(1), 39–50 (1992).
- <sup>45</sup>R. Govardhan and C. H. K. Williamson, "Modes of vortex formation and frequency response for a freely-vibrating cylinder," *J. Fluid Mech.* **420**, 85–130 (2000).
- <sup>46</sup>N. Almarri, J. Chang, W. Song, D. Jiang, and A. Demosthenous, "Piezoelectric energy harvesting and ultra-low-power management circuits for medical devices," *Nano Energy* **131**, 110196 (2024).
- <sup>47</sup>Y. Liao and H. A. Sodano, "Model of a single mode energy harvester and properties for optimal power generation," *Smart Mater. Struct.* **17**(6), 065026 (2008).